

# A factorization approach of the mixed dynamic form factor for mapping atomic orbitals

S. Löffler<sup>a</sup>, V. Motsch<sup>a</sup>, P. Schattschneider<sup>a,b</sup>

<sup>a</sup>*Institute of Solid State Physics, Vienna University of Technology, Vienna, Austria*

<sup>b</sup>*University Service Centre for Electron Microscopy, Vienna University of Technology, Vienna, Austria*

## Abstract

We demonstrate how the mixed dynamic form factor (MDFF) can be interpreted as a quadratic form. This makes it possible to use matrix diagonalization methods to reduce the number of terms that need to be taken into account when calculating the inelastic scattering of electrons in a crystal. It also leads in a natural way to a new basis that helps elucidate the underlying physics. The new method is applied to several cases to show its versatility. In particular, predictions are made for directly imaging atomic orbitals in crystals.

**Keywords:** inelastic scattering, mixed dynamic form factor, orbital mapping

## 1. Introduction

Nowadays, simulations are indispensable both for planning and for interpreting experiments in the transmission electron microscope (TEM), in particular when working with electron energy loss spectrometry (EELS). The key quantity for simulating inelastic electron scattering is the mixed dynamic form factor (MDFF) [1–3]. In many cases, this complex quantity is simplified by several approximations, like, for instance, the dipole approximation. Recently, it has been shown, however, that this can lead to quite severe errors [4]. Furthermore, with recent advances of aberration corrected microscopes, more accurate calculations of the MDFF will become essential for future experiments.

In this work, we will give a brief repetition of the mixed dynamic form factor, followed by an analysis of how a basis transformation can bring it into a simpler form that is much better to handle numerically. Furthermore, the physical significance of this procedure will be outlined. In the last part, the new formalism will be applied to both existing and new measurement setups to study its applicability and versatility.

## 2. The mixed dynamic form factor and its factorization

In the most general approach, the quantum mechanical system consisting of both the probe electron and the sample can best be described by a density operator  $\hat{\rho}$  or its matrix elements, the so-called density matrix  $\rho$  [5]. Adopting the density matrix formalism instead of the simpler wave

function approach is greatly beneficial as one cannot observe the target's final state directly. This ignorance of a part of the system after an inelastic interaction gives rise to a mixed state which can be described very effectively using the density matrix [2, 3, 5].

Before the interaction, the probe and the target system can be considered independent. For the sake of simplicity, we will furthermore assume that both systems are initially in a pure state, i.e., each can be described by a single wave function. Then, the density operator of the whole system before the interaction

$$\hat{\rho}_{\text{tot},0} = |i\rangle\langle i| \otimes |I\rangle\langle I| = |I\rangle\langle I| |i\rangle\langle i|, \quad (1)$$

where  $\otimes$  denotes the direct product. Throughout this article, we use small letters when referring to the probe beam and capital letters when referring to the target.

In first order Born approximation, the density operator after the inelastic interaction mediated by an interaction potential  $\hat{V}$  is given by

$$\hat{\rho}_{\text{tot}} = \hat{V} |I\rangle\langle i| \langle i| \langle I| \hat{V}^\dagger. \quad (2)$$

Since the target system is not observed directly, one has to construct the reduced density operator for the probe beam by summing incoherently over all possible final states of the target. This reduced density operator is given by

$$\hat{\rho} = \sum_F \langle F| \hat{V} |I\rangle |i\rangle\langle i| \langle I| \hat{V}^\dagger |F\rangle, \quad (3)$$

which can then be propagated elastically through the crystal and be used to predict the outcome of measurements in different geometries. It must be emphasized that the ordering of the terms is vital here, since  $\hat{V}$  in general acts on both the probe and the target states, which results in an entanglement of the two.

Email address: stefan.loeffler@tuwien.ac.at (S. Löffler)

In EELS experiments, the interaction operator  $\hat{V}$  is the Coulomb interaction operator. Its two most common basis representations are in configuration space,

$$\begin{aligned}\hat{V}(\mathbf{r}, \mathbf{r}') &= \langle \mathbf{r} | \hat{V} | \mathbf{r}' \rangle = \frac{\delta(\hat{\mathbf{R}} - \hat{\mathbf{R}}')}{|\mathbf{r} - \hat{\mathbf{R}}|} \delta(\mathbf{r} - \mathbf{r}') \delta(E_I - E_F + E) \\ &=: \hat{V}(\mathbf{r}) \delta(\mathbf{r} - \mathbf{r}'),\end{aligned}\quad (4)$$

and in reciprocal space,

$$\begin{aligned}\hat{V}(\mathbf{k}, \mathbf{k}') &= \langle \mathbf{k} | \hat{V} | \mathbf{k}' \rangle = \frac{e^{i(\mathbf{k}' - \mathbf{k}) \cdot \hat{\mathbf{R}}}}{|\mathbf{k}' - \mathbf{k}|^2} \delta(\hat{\mathbf{R}} - \hat{\mathbf{R}}') \delta(E_I - E_F + E) \\ &= \frac{e^{i\mathbf{q} \cdot \hat{\mathbf{R}}}}{|\mathbf{q}|^2} \delta(\hat{\mathbf{R}} - \hat{\mathbf{R}}') \delta(E_I - E_F + E) \\ &=: \hat{V}(\mathbf{q}).\end{aligned}\quad (5)$$

The constant prefactors were omitted for the sake of clarity.  $E_I, E_F$  denote the energies of the target's initial and final states, respectively, and  $E$  is the energy loss of the probe electron.

In these two representations, the reduced density operator reads

$$\begin{aligned}\rho(\mathbf{r}, \mathbf{r}') &= \sum_F \int d\tilde{\mathbf{r}} \langle F | \langle \mathbf{r} | \hat{V} | \tilde{\mathbf{r}} \rangle | I \rangle \langle \tilde{\mathbf{r}} | i \rangle \\ &\quad \int d\tilde{\mathbf{r}}' \langle i | \tilde{\mathbf{r}}' \rangle \langle I | \langle \tilde{\mathbf{r}}' | \hat{V}^\dagger | \mathbf{r}' \rangle | F \rangle \\ &= \sum_F \langle F | \hat{V}(\mathbf{r}) | I \rangle \langle I | \hat{V}^\dagger(\mathbf{r}') | F \rangle \langle \mathbf{r} | i \rangle \langle i | \mathbf{r}' \rangle \\ &= S(\mathbf{r}, \mathbf{r}') \langle \mathbf{r} | i \rangle \langle i | \mathbf{r}' \rangle \\ \rho(\mathbf{k}, \mathbf{k}') &= \sum_F \int d\tilde{\mathbf{k}} \langle F | \langle \mathbf{k} | \hat{V} | \tilde{\mathbf{k}} \rangle | I \rangle \langle \tilde{\mathbf{k}} | i \rangle \\ &\quad \int d\tilde{\mathbf{k}}' \langle i | \tilde{\mathbf{k}}' \rangle \langle I | \langle \tilde{\mathbf{k}}' | \hat{V}^\dagger | \mathbf{k}' \rangle | F \rangle \\ &= \sum_F \iint d\mathbf{q} d\mathbf{q}' \langle F | \hat{V}(\mathbf{q}) | I \rangle \langle I | \hat{V}^\dagger(\mathbf{q}') | F \rangle \\ &\quad \langle \mathbf{k} + \mathbf{q} | i \rangle \langle i | \mathbf{k}' + \mathbf{q}' \rangle \\ &= \iint d\mathbf{q} d\mathbf{q}' S(\mathbf{q}, \mathbf{q}') \langle \mathbf{k} + \mathbf{q} | i \rangle \langle i | \mathbf{k}' + \mathbf{q}' \rangle.\end{aligned}\quad (6)$$

Here, the MDFF  $S(\mathbf{q}, \mathbf{q}')$  and the real-space MDFF (rMDFF)  $S(\mathbf{r}, \mathbf{r}')$  were introduced which are related by a Fourier transformation<sup>1</sup>. It is noteworthy that — due to the particular properties of the Coulomb operator — the rMDFF can be multiplied on the initial probe wave functions, whereas the MDFF has to be convolved with them.

In order to perform calculations, one not only has to specify a basis for the probe states, but also for the target states. Usually, one chooses a spherical harmonics basis which is particularly useful for describing the tightly

bound initial states that give rise to EELS core losses. Hence, the initial state written as  $|l\frac{1}{2}jj_z\rangle^2$ , while the final states are expanded in terms of  $|LM\frac{1}{2}S\rangle$ . In the following, we will also sum incoherently over  $j_z$  since that quantum number of the initial state is typically unknown. In the Kohn-Sham approximation, the MDFF is then given by [6–8]

$$\begin{aligned}S(\mathbf{q}, \mathbf{q}') &= \sum_{Fj_z} \sum_{LMSL'M'S'} \langle F | LM\frac{1}{2}S \rangle \langle LM\frac{1}{2}S | \hat{V}(\mathbf{q}) | l\frac{1}{2}jj_z \rangle \\ &\quad \langle l\frac{1}{2}jj_z | \hat{V}^\dagger(\mathbf{q}') | L'M'\frac{1}{2}S' \rangle \langle L'M'\frac{1}{2}S' | F \rangle \\ &= \frac{4\pi}{q^2 q'^2} (2l+1)(2j+1) \sum_{mm'} \sum_{LMS} \sum_{L'M'S'} \sum_{\lambda\mu\lambda'\mu'} \\ &\quad i^{\lambda-\lambda'} \sqrt{(2\lambda+1)(2\lambda'+1)(2L+1)(2L'+1)} \\ &\quad Y_\lambda^\mu(\mathbf{q})^* \langle j_\lambda(q) \rangle_{EL Sj} Y_{\lambda'}^{\mu'}(\mathbf{q}') \langle j_{\lambda'}(q') \rangle_{EL' S' j} \\ &\quad \begin{pmatrix} l & \lambda & L \\ 0 & 0 & 0 \end{pmatrix} \begin{pmatrix} l & \lambda' & L' \\ 0 & 0 & 0 \end{pmatrix} \\ &\quad \begin{pmatrix} l & \lambda & L \\ -m & \mu & M \end{pmatrix} \begin{pmatrix} l & \lambda' & L' \\ -m' & \mu' & M' \end{pmatrix} \\ &\quad \sum_{j_z} (-1)^{m+m'} \begin{pmatrix} l & \frac{1}{2} & j \\ m & S & -j_z \end{pmatrix} \begin{pmatrix} l & \frac{1}{2} & j \\ m' & S' & -j_z \end{pmatrix} \\ &\quad \sum_{\mathbf{k}n} D_{LMS}^{\mathbf{k}n} (D_{L'M'S'}^{\mathbf{k}n})^* \delta(E + E_{nl\kappa} - E_{\mathbf{k}n}).\end{aligned}\quad (7)$$

Here,

$$\langle j_\lambda(q) \rangle_{EL Sj} = \int u_{LS}^E(r) j_\lambda(qr) R_{lj}(r) r^2 dr \quad (8)$$

is the weighted radial wave function overlap [6, 9] with the initial state's radial wave function  $R_j(r)$ , the final state's radial wave function  $u_{LS}^E(r)$  and the spherical Bessel function  $j_\lambda$ . The  $\sum_{\mathbf{k}n} D_{LMS}^{\mathbf{k}n} (D_{L'M'S'}^{\mathbf{k}n})^*$  is the cross density of states (XDOS) and the  $\begin{pmatrix} \cdot & \cdot & \cdot \\ \cdot & \cdot & \cdot \end{pmatrix}$  are Wigner 3j symbols.

While this choice of basis is very convenient as a starting point (as it is used, e.g., in WIEN2k [10]), it is by no means the only or the optimal choice. This can be seen by collecting terms depending on  $\mathbf{q}$  and terms depending on

<sup>1</sup>Contrary to the convention adopted in previous works, we include the  $1/q^2 q'^2$  term in the definition of the MDFF as it makes the definition more concise and easy to use.

<sup>2</sup>This takes into account the spin-orbit coupling of the tightly bound core states

$\mathbf{q}'$ . With the abbreviations

$$\begin{aligned}
\alpha &= (\lambda, \mu, L, S) \\
\alpha' &= (\lambda', \mu', L', S') \\
\mathbf{g}_\alpha(\mathbf{q}) &= \frac{1}{q^2} Y_\lambda^\mu(\mathbf{q}) \langle j_\lambda(q) \rangle_{EL S j} \\
\Xi_{\alpha\alpha'} &= 4\pi(2l+1)(2j+1) \sum_{mm'} \sum_{MM'} \\
&\quad i^{\lambda-\lambda'} \sqrt{(2\lambda+1)(2\lambda'+1)(2L+1)(2L'+1)} \\
&\quad \begin{pmatrix} l & \lambda & L \\ 0 & 0 & 0 \end{pmatrix} \begin{pmatrix} l & \lambda' & L' \\ 0 & 0 & 0 \end{pmatrix} \\
&\quad \begin{pmatrix} l & \lambda & L \\ -m & \mu & M \end{pmatrix} \begin{pmatrix} l & \lambda' & L' \\ -m' & \mu' & M' \end{pmatrix} \\
&\quad \sum_{j_z} (-1)^{m+m'} \begin{pmatrix} l & \frac{1}{2} & j \\ m & S & -j_z \end{pmatrix} \begin{pmatrix} l & \frac{1}{2} & j \\ m' & S' & -j_z \end{pmatrix} \\
&\quad \sum_{\mathbf{k}n} D_{LMS}^{\mathbf{k}n} (D_{L'M'S'}^{\mathbf{k}n})^* \delta(E + E_{n\mathbf{k}} - E_{\mathbf{k}n}),
\end{aligned} \tag{9}$$

the MDFF can be rewritten as

$$\begin{aligned}
S(\mathbf{q}, \mathbf{q}') &= \sum_{\alpha\alpha'} g_\alpha(\mathbf{q})^\dagger \Xi_{\alpha\alpha'} g_{\alpha'}(\mathbf{q}') \\
&= \mathbf{g}(\mathbf{q})^\dagger \cdot \Xi \cdot \mathbf{g}(\mathbf{q}'),
\end{aligned} \tag{10}$$

where the matrix  $\Xi$  collects all  $\mathbf{q}, \mathbf{q}'$  independent terms and can be computed in a straight-forward way once the XDOS is known (e.g., from DFT calculations). The  $\mathbf{g}$  in turn can be interpreted as a vector of functions. This is a well-known quadratic form. In particular,  $\Xi$  is hermitian (as is shown in Appendix A).

With the default settings, WIEN2k produces data with  $0 \leq L, L' \leq 3$ . When including transitions up to quadrupole order ( $\lambda = 2$ ),  $\Xi$  is a  $72 \times 72$  matrix, resulting in up to 5184 terms in the MDFF that in principle would all have to be handled separately. In practice, some of the entries vanish due to selection rules, while for some others the hermiticity of  $\Xi$  can be exploited. Still, many off-diagonal elements generally remain. These off-diagonal elements imply correlations between the basis vectors [3] and hence represent additional information (e.g., symmetries) about the underlying system that can be used to simplify the problem.

To exploit this additional information, one can insert unitary matrices  $\mathbf{U}$  in the following way:

$$S(\mathbf{q}, \mathbf{q}') = \mathbf{g}(\mathbf{q})^\dagger \cdot \mathbf{U}^\dagger \mathbf{U} \cdot \Xi \cdot \mathbf{U}^\dagger \mathbf{U} \cdot \mathbf{g}(\mathbf{q}'). \tag{11}$$

Since for any hermitian matrix, a unitarian matrix exists such that  $\mathbf{U}\Xi\mathbf{U}^\dagger$  is a diagonal matrix  $\mathbf{D}$ , one only has to find such a  $\mathbf{U}$ . This is straight forward using, e.g., eigenvalue solvers, a singular value decomposition, or a Schur decomposition. With the abbreviation  $\tilde{\mathbf{g}}(\mathbf{q}) = \mathbf{U} \cdot \mathbf{g}(\mathbf{q})$ , the MDFF becomes

$$S(\mathbf{q}, \mathbf{q}') = \tilde{\mathbf{g}}(\mathbf{q})^\dagger \cdot \mathbf{D} \cdot \tilde{\mathbf{g}}(\mathbf{q}'). \tag{12}$$

In terms of quadratic forms, the transformation  $\mathbf{U}$  is a principal axis transformation. In quantum mechanical terms, it is a basis transformation into the eigensystem of the MDFF. In essence, it recovers the “physical” basis of independent — i.e., uncorrelated because of vanishing off-diagonal terms — transitions.<sup>3</sup> With the default settings of WIEN2k, this means that the problem was reduced from at most 5184 terms to at most 72 terms.

In numerical simulations, it is usually beneficial to work with the rMDFF as it can be multiplied directly onto the incident density matrix. Since the rMDFF is related to the MDFF by a Fourier transformation and the  $\mathbf{q}$  and  $\mathbf{q}'$  dependencies have been decoupled, the rMDFF simply reads

$$S(\mathbf{r}, \mathbf{r}') = \tilde{\mathbf{g}}(\mathbf{r})^\dagger \cdot \mathbf{D} \cdot \tilde{\mathbf{g}}(\mathbf{r}') \tag{13}$$

with the same matrix  $\mathbf{D}$  as for the MDFF and  $\tilde{\mathbf{g}}(\mathbf{r}) = FT_{\mathbf{q}}[\tilde{\mathbf{g}}(\mathbf{q})]$ . By renormalizing the  $\tilde{\mathbf{g}}$  such that  $\bar{g}_\alpha(\mathbf{r}) := \sqrt{D_{\alpha\alpha}} \tilde{g}_\alpha(\mathbf{r})$ , the MDFF can be further simplified to

$$S(\mathbf{r}, \mathbf{r}') = \bar{\mathbf{g}}(\mathbf{r})^\dagger \cdot \bar{\mathbf{g}}(\mathbf{r}') = \sum_{\alpha} \bar{g}_\alpha(\mathbf{r})^* \bar{g}_\alpha(\mathbf{r}') \tag{14}$$

Hence, the reduced density matrix of the probe electron after the inelastic interaction in configuration space can be written as

$$\rho(\mathbf{r}, \mathbf{r}') = \sum_{\alpha} (\bar{g}_\alpha(\mathbf{r}) \phi(\mathbf{r}))^* \bar{g}_\alpha(\mathbf{r}') \phi(\mathbf{r}'), \tag{15}$$

where we wrote  $\phi(\mathbf{r}) = \langle \mathbf{r} | i \rangle$  for the incident probe electron wave function. It is quite obvious that the diagonalization of the rMDFF has resulted in a factorization of the density operator  $\hat{\rho} = \sum_{\alpha} |\alpha\rangle \langle \alpha|$ . Finally — when measuring a real space image —, the measurable intensity  $I$  is given by<sup>4</sup>

$$I(\mathbf{r}) = \rho(\mathbf{r}, \mathbf{r}) = \sum_{\alpha} |\bar{g}_\alpha(\mathbf{r}) \phi(\mathbf{r})|^2 \tag{16}$$

In the description above, elastic scattering of the probe beam after the inelastic scattering event has not been included for the sake of simplicity. Since each  $|\alpha\rangle$  in itself is a pure state, it can be propagated elastically through the rest of the crystal with existing methods (e.g., the multislice approach [11]), however. While this does change the image, of course, it does not change the underlying physics, or the coherence properties and the general statements made above still hold.

<sup>3</sup>Note that, depending on the EELS-edge and multipole orders considered, it may or may not be possible to determine the target’s “physical” basis  $|F\rangle$  from these transitions. Considering, e.g., a dipole-allowed transition from an initial p state to a final d state, one has only three transition elements ( $\mu \in \{-1, 0, 1\}$ ), but 5 final states. Under these circumstances, not all information about the final states can be probed, unless one takes into account other multipole orders or final states.

<sup>4</sup>Here, an ideal lens system was assumed. Real lenses will reduce the level of detail transferred to the image, but do not change the coherence properties of the partial waves.

### 3. Applications

#### 3.1. Single atom

For single, individual atoms, all final states are independent of one another and hence uncorrelated. In addition, in the absence of a (strong) external magnetic field, states with the same  $L$ , but different  $M$  or  $S$  can be considered degenerate. For the XDOS, this means

$$\sum_{kn} D_{LMS}^{kn} (D_{L'M'S'}^{kn})^* = D_L \delta_{LL'} \delta_{MM'} \delta_{SS'}. \quad (17)$$

In the case of no spin-polarization, the  $\langle j_\lambda \rangle$  also do not depend on  $S$  and the sum over  $S, S'$  can be carried out and the spin-dependence of  $\alpha$  can be dropped. Using the orthogonality relations for the Wigner 3j symbols, a short calculation then yields

$$\Xi_{\alpha\alpha'} = 4\pi(2L+1)(2j+1) \begin{pmatrix} l & \lambda & L \\ 0 & 0 & 0 \end{pmatrix}^2 D_L \delta_{\lambda\lambda'} \delta_{\mu\mu'} \delta_{LL'}, \quad (18)$$

Hence, for single, isolated atoms,  $\Xi$  is diagonal, i.e., no correlations occur, even in the untransformed basis. Also note that all  $\mu$  have the same weighting, i.e., any basis transform that only mixes the different  $\mu$  of any given  $\lambda$  but does not mix the  $\lambda$  or  $L$  blocks leaves  $\Xi$  unchanged. Owing to the incoherent summation over different  $|\alpha\rangle$  in eq. 16, in the real space image this ultimately leads to terms of the form<sup>5</sup>  $\sum_{\mu} |e^{i\mu\varphi}|^2 = 1$  [12] which gives rise to circular intensity profiles regardless of the symmetries of the target's initial or final states.

#### 3.2. Energy-loss magnetic chiral dichroism

Since its discovery in 2006 [6], interest in the energy loss magnetic chiral dichroism (EMCD) technique has been growing steadily. Using EMCD, one can determine the magnetic properties of the sample [13], similar to the X-ray magnetic circular dichroism which is a standard method in the synchrotron. The factorization approach outlined here can also be applied to EMCD.

For the sake of simplicity, we assume here a fully spin-polarized ( $\delta_{S\frac{1}{2}}\delta_{S'\frac{1}{2}}$ ) dipole-allowed ( $\lambda = \lambda' = 1$ ) transition from an initial p ( $l = 1$ ) to a final d ( $L = L' = 2$ ) state, as is the dominant contribution to the L-edge in most common magnetic materials. In addition, we assume that states with same  $L$ , but different  $M$  are (mostly) degenerate, as in the isolated atom case. Hence, the XDOS reads

$$\sum_{kn} D_{LMS}^{kn} (D_{L'M'S'}^{kn})^* = D_2 \delta_{L2} \delta_{L'2} \delta_{MM'} \delta_{S\frac{1}{2}} \delta_{S'\frac{1}{2}}. \quad (19)$$

Under these assumptions,  $\Xi$  becomes a  $3 \times 3$  matrix for both  $j = 1/2$  (corresponding to the  $L_2$  edge) and  $j = 3/2$

(corresponding to the  $L_3$  edge):

$$\begin{aligned} \Xi_{j=1/2} &= \frac{4\pi D_2}{3} \begin{pmatrix} 1 & 0 & 0 \\ 0 & 2 & 0 \\ 0 & 0 & 3 \end{pmatrix} \\ \Xi_{j=3/2} &= \frac{4\pi D_2}{3} \begin{pmatrix} 5 & 0 & 0 \\ 0 & 4 & 0 \\ 0 & 0 & 3 \end{pmatrix} \end{aligned} \quad (20)$$

As in the single-atom case,  $\Xi$  is already diagonal in the spherical harmonics basis. Here, however, different  $\mu$  have different weights. This means that transforming to any other basis will introduce off-diagonal elements (only the identity matrix is invariant under rotations). Hence, the spherical harmonics basis is the only “physical” basis for EMCD.

Moreover, the  $\Xi$  matrices given above can be interpreted as a homogeneous average signal on which the  $\mu$ -dependent EMCD signal is superimposed:

$$\begin{aligned} \Xi_{j=1/2} &= \frac{4\pi D_2}{3} \left[ \begin{pmatrix} 2 & 0 & 0 \\ 0 & 2 & 0 \\ 0 & 0 & 2 \end{pmatrix} + \begin{pmatrix} -1 & 0 & 0 \\ 0 & 0 & 0 \\ 0 & 0 & 1 \end{pmatrix} \right] \\ \Xi_{j=3/2} &= \frac{4\pi D_2}{3} \left[ \begin{pmatrix} 4 & 0 & 0 \\ 0 & 4 & 0 \\ 0 & 0 & 4 \end{pmatrix} + \begin{pmatrix} 1 & 0 & 0 \\ 0 & 0 & 0 \\ 0 & 0 & -1 \end{pmatrix} \right] \end{aligned} \quad (21)$$

This immediately shows two features common to EELS and EMCD. On the one hand, the homogeneous average signal exhibits the typical, statistical 1:2 intensity ratio of the  $L_2:L_3$  edges. On the other hand, the EMCD signal (the absolute magnitude of which is independent of  $j$  in this simple case) shows the typical sign reversal between  $L_2$  and  $L_3$  edges.

#### 3.3. Crystals

In crystals, the situation is more complicated and simple toy-models are insufficient to grasp them completely. Hence, one needs sophisticated calculations to derive the XDOS that take into account the full crystal structure. Analogous to the examples given above (in particular to the isolated atom case), one can argue that for high-symmetry crystals (such as cubic systems), the XDOS may become diagonal in  $M, M'$  [8, 14] and hence many of the cross-terms vanish.<sup>6</sup>

Hence, we will use the Oxygen K-edge of Rutile ( $\text{TiO}_2$ ), a tetragonal system, as test case in this work. Fig. 1a shows a schematic of the unit cell, while fig. 1b shows the partial density of states (pDOS) for Oxygen as calculated by WIEN2k. From it, the lifting of the degeneracy of the different p orbitals is already evident.

For this system, WIEN2k produces 89 non-negligible<sup>7</sup> XDOS components at  $E_F + 4$  eV, whereas at  $E_F + 7$  eV it

<sup>5</sup>Assuming elastic scattering effects are negligible.

<sup>6</sup>The complete investigation of the effects of crystal symmetries on the XDOS and  $\Xi$  is beyond the scope of this work.

<sup>7</sup>Here, elements are considered non-negligible if they are larger than 1‰ of the largest element

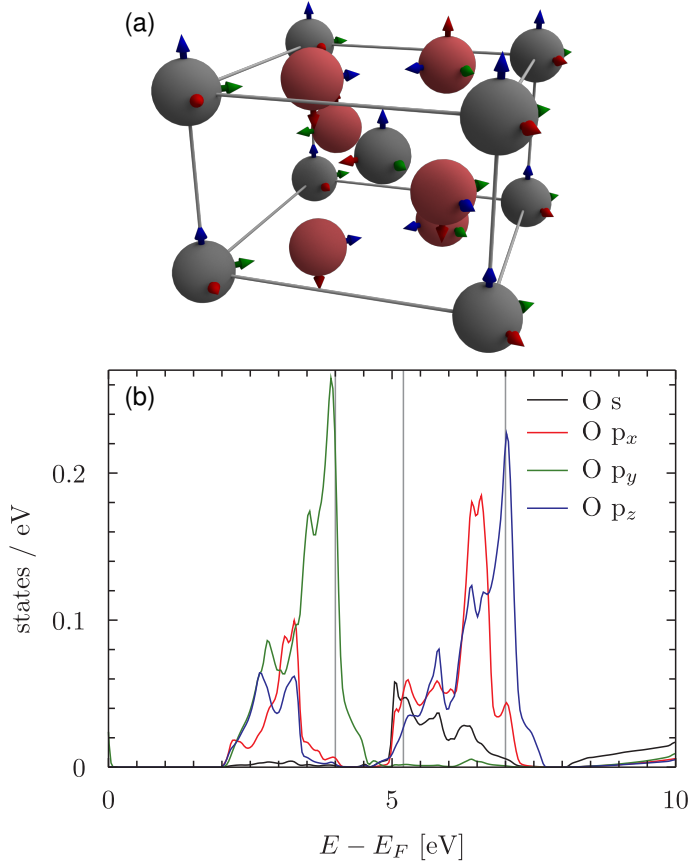


Figure 1: (a) schematic of the unit cell for Rutile (gray: Ti, red: O). The lattice constants are  $a = 4.594$  Å and  $c = 2.958$  Å. The arrows show the symmetry-adapted local coordinate systems (red: x, green: y, blue: z). (b) pDOS of the Oxygen p-states as calculated by WIEN2k. The gray bars show energies used for simulations in this work.

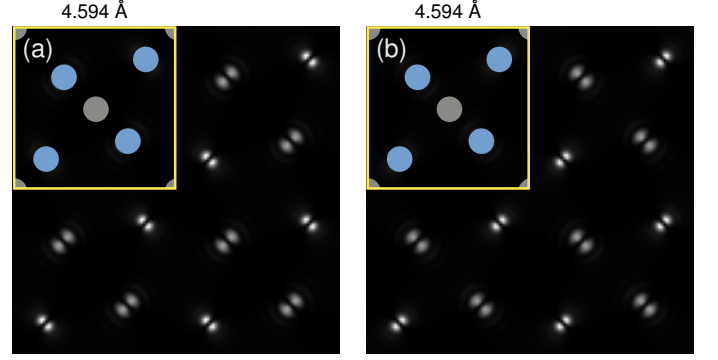


Figure 2: Real-space intensity of the exit wave after propagation of an incident plane wave through a one unit-cell thick crystal oriented in  $[001]$  zone axis at 200 kV acceleration voltage. Only dipole-allowed transitions were taken into account. (a) shows the image at an energy loss of  $E_F + 4$  eV, whereas (b) shows the image at an energy loss of  $E_F + 7$  eV. The inset shows the projected unit cell with Ti atoms in gray and O atoms in blue.

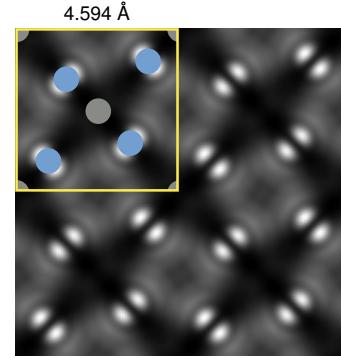


Figure 3: Real-space intensity of the exit wave after propagation of an incident plane wave through a 10 nm thick crystal oriented in  $[001]$  zone axis at 200 kV acceleration voltage. A 24 mrad objective aperture was used. Only dipole-allowed transitions were taken into account. The image is taken at an energy loss of  $E_F + 4$  eV. The inset shows the projected unit cell with Ti atoms in gray and O atoms in blue.

produces 100 non-negligible elements in the spin-unpolarized case. In the simplest case of taking into account only dipole-allowed transitions ( $\lambda = \lambda' = 1$ ), the  $3 \times 3$  matrix  $\Xi$  has 5 non-vanishing entries, which are reduced to 3 after diagonalization.

Fig. 2a shows the simulated exit wave function intensities (corresponding to an ideal lens system) for a single unit cell after an energy loss of  $E_F + 4$  eV. The Oxygen  $p_y$  orbitals are clearly visible to be pointing in the directions of the green axes in fig. 1a.

Likewise, fig. 2b shows the simulated exit wave function intensities at an energy loss of  $E_F + 7$  eV. There, the Oxygen  $p_z$  orbitals are clearly visible. They naturally are rotated by  $90^\circ$  with respect to the  $p_y$  orbitals and are pointing in the direction of the blue axes in fig. 1a.

Fig. 3 shows the situation for a 10 nm thick crystal and an objective aperture of 24 mrad. It demonstrates that these results are not only of theoretical interest, but should be measurable in real instruments. The contrast

can be estimated to be 96 % (after subtraction of the pre-edge background, e.g., using the three-window method).

More importantly, non-dipole transitions can easily be taken into account as well. For the Oxygen K-edge, the most relevant non-dipole transition is the monopole transition from the 1s state to final states with s symmetry<sup>8</sup>. Here, the number of non-negligible terms was reduced from 10 to 4. Fig. 4 compares the intensities and images of monopole-allowed transitions, dipole-allowed transitions, and the coupling term between the two. A similar effect was predicted recently for X-ray absorption spectrometry [15].

Interestingly, the coupling term gives intensity variations of almost  $\pm 20$  % of the dipole-allowed transitions and is much larger than the monopole transitions themselves. This acts in a way very similar to s-p hybridization, yielding an asymmetric image.

#### 4. Conclusion and Outlook

In this work, we demonstrated a method to factorize both the MDFF and the rMDFF by means of a matrix diagonalization. This was shown to yield obvious numerical advantages by reducing the number of terms to include in image calculations. Moreover, the diagonalization leads to a new set of basis vectors that are helpful to elucidate the physics underlying the scattering process.

The new factorization method was applied to the isolated atom case, EMCD, and a Rutile crystal to show its versatility. In particular, the isolated atom and the EMCD cases could be treated analytically, giving results from which important properties such as the  $L_2:L_3$  ratio or the sign reversal of the EMCD effect could be seen immediately.

For the Rutile crystal, it was shown that with latest-generation TEMs, it should be possible to directly map atomic orbitals, e.g., using energy filtered TEM (EFTEM) with high spatial resolution. However, contrary to the common assumption that non-dipole transitions are unimportant, it was shown that particularly the monopole-dipole coupling term can change the measured signal significantly.

This new technique gives rise to exciting new possibilities. For example, it could be used to directly study the electronic structure of defects, interfaces, or other low-symmetry objects.

#### Acknowledgements

The authors acknowledge financial support by the Austrian Science Fund (FWF) under grant number I543-N20. They also want to express their gratitude to Walid Hetaba for fruitful discussions about and help using WIEN2k.

<sup>8</sup>The pDOS for d states as produced by WIEN2k that would be accessible by quadrupole-allowed transitions is negligibly small.

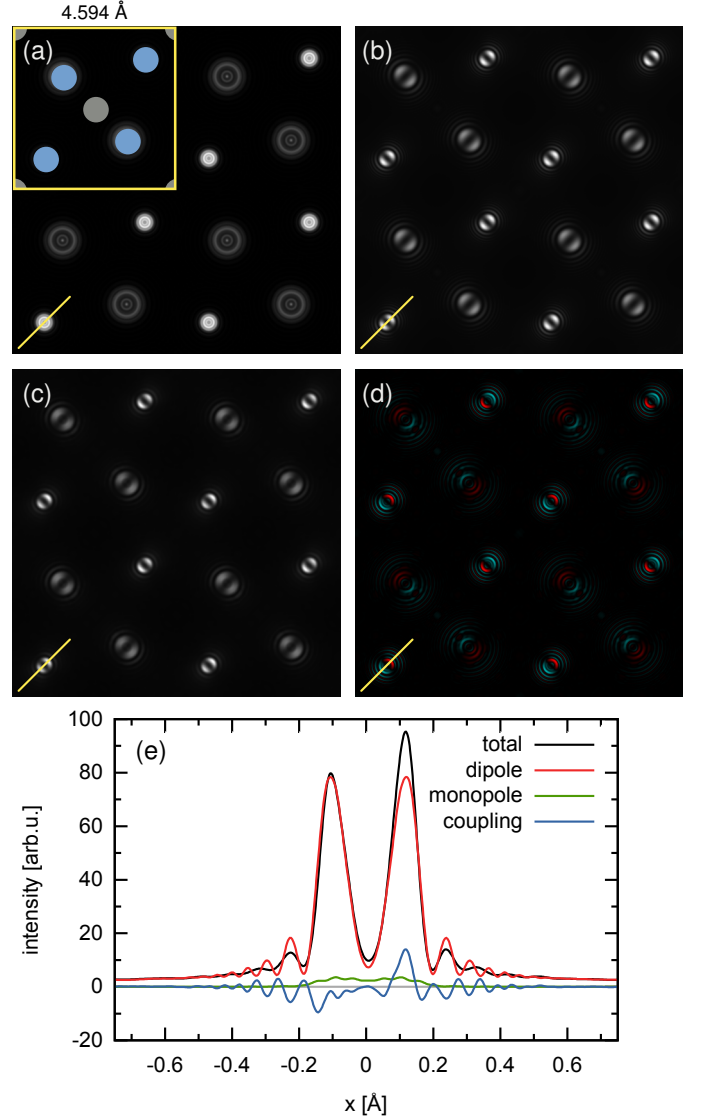


Figure 4: (a) - (d) Real-space intensities of the exit wave after propagation of an incident plane wave through a one unit cell thick crystal oriented in  $[00\ 1]$  zone axis at 200 kV acceleration voltage. (a) shows only monopole contributions (contrast-enhanced by a factor of 25), (b) shows only dipole contributions (contrast-enhanced by a factor of 1.2), (c) shows the total intensity, and (d) shows the coupling contribution (contrast enhanced by a factor of 7; red indicates positive values while cyan represents negative ones). The images are taken at an energy loss of  $E_F + 5.2$  eV. The inset shows the projected unit cell with Ti atoms in gray and O atoms in blue. (e) Traces of the different contributions. The places of the trace are marked by yellow lines

## Appendix A. Hermiticity of $\Xi$

For  $\Xi$  to be hermitian, the equation

$$\Xi_{\alpha'\alpha} = \Xi_{\alpha\alpha'}^* \quad (\text{A.1})$$

must hold.

$$\begin{aligned} \Xi_{\alpha'\alpha} &= 4\pi(2l+1)(2j+1) \sum_{m'm} \sum_{M'M} \delta(E + E_{nl\kappa} - E_{\mathbf{k}n}) \\ &\quad \sqrt{(2\lambda'+1)(2\lambda+1)(2L'+1)(2L+1)} \\ &\quad \begin{pmatrix} l & \lambda' & L' \\ 0 & 0 & 0 \end{pmatrix} \begin{pmatrix} l & \lambda & L \\ 0 & 0 & 0 \end{pmatrix} \\ &\quad \begin{pmatrix} l & \lambda' & L' \\ -m' & \mu' & M' \end{pmatrix} \begin{pmatrix} l & \lambda & L \\ -m & \mu & M \end{pmatrix} \\ &\quad \sum_{j_z} (-1)^{m'+m} \begin{pmatrix} l & \frac{1}{2} & j \\ m' & S' & -j_z \end{pmatrix} \begin{pmatrix} l & \frac{1}{2} & j \\ m & S & -j_z \end{pmatrix} \\ &\quad i^{\lambda'-\lambda} \sum_{\mathbf{k}n} D_{L'M'S'}^{\mathbf{k}n} (D_{LMS}^{\mathbf{k}n})^* \\ &= 4\pi(2l+1)(2j+1) \sum_{mm'} \sum_{MM'} \delta(E + E_{nl\kappa} - E_{\mathbf{k}n}) \\ &\quad \sqrt{(2\lambda+1)(2\lambda'+1)(2L+1)(2L'+1)} \\ &\quad \begin{pmatrix} l & \lambda & L \\ 0 & 0 & 0 \end{pmatrix} \begin{pmatrix} l & \lambda' & L' \\ 0 & 0 & 0 \end{pmatrix} \\ &\quad \begin{pmatrix} l & \lambda & L \\ -m & \mu & M \end{pmatrix} \begin{pmatrix} l & \lambda' & L' \\ -m' & \mu' & M' \end{pmatrix} \\ &\quad \sum_{j_z} (-1)^{m+m'} \begin{pmatrix} l & \frac{1}{2} & j \\ m & S & -j_z \end{pmatrix} \begin{pmatrix} l & \frac{1}{2} & j \\ m' & S' & -j_z \end{pmatrix} \\ &\quad \left[ i^{\lambda-\lambda'} \sum_{\mathbf{k}n} D_{LMS}^{\mathbf{k}n} (D_{L'M'S'}^{\mathbf{k}n})^* \right]^* \\ &= \Xi_{\alpha\alpha'}^* \end{aligned} \quad (\text{A.2})$$

## Bibliography

### References

- [1] H. Kohl and H. Rose. Theory of image formation by inelastically scattered electrons in the electron microscope. In Peter W. Hawkes, editor, *Advances in Electronics and Electron Physics*, volume 65 of *Advances in Electronics and Electron Physics*, pages 173 – 227. Academic Press, 1985. doi: 10.1016/S0065-2539(08)60878-1.
- [2] P. Schattschneider, M. Nelhiebel, and B. Jouffrey. Density matrix of inelastically scattered fast electrons. *Phys. Rev. B*, 59(16):10959–10969, Apr 1999. doi: 10.1103/PhysRevB.59.10959.
- [3] P. Schattschneider, M. Nelhiebel, H. Souchay, and B. Jouffrey. The physical significance of the mixed dynamic form factor. *Micron*, 31(4):333 – 345, 2000. ISSN 0968-4328. doi: 10.1016/S0968-4328(99)00112-2.
- [4] Stefan Löffler, Inga Ennen, Feng Tian, Peter Schattschneider, and Nicolas Jaouen. Breakdown of the dipole approximation in core losses. *Ultramicroscopy*, 111:1163 – 1167, 2011. doi: 10.1016/j.ultramic.2011.03.006.
- [5] Karl Blum. *Density Matrix Theory and Applications*. Physics of Atoms and Molecules. Springer, 2nd edition, 1996. ISBN 0-306-45341-X.

- [6] P. Schattschneider, S. Rubino, C. Hebert, J. Rusz, J. Kunes, P. Novák, E. Carlino, M. Fabrizioli, G. Panaccione, and G. Rossi. Detection of magnetic circular dichroism using a transmission electron microscope. *Nature*, 441:486–488, 2006. doi: 10.1038/nature04778.
- [7] Ján Rusz, Stefano Rubino, and Peter Schattschneider. First-principles theory of chiral dichroism in electron microscopy applied to 3d ferromagnets. *Phys. Rev. B*, 75(21):214425, 2007. doi: 10.1103/PhysRevB.75.214425.
- [8] Michael Nelhiebel. *Effects of crystal orientation and interferometry in electron energy loss spectroscopy*. PhD thesis, cole Centrale Paris, Châtenay-Malabry, may 1999.
- [9] Stefan Löffler and Peter Schattschneider. Transition probability functions for applications of inelastic electron scattering. *Micron*, 43(9):971 – 977, 2012. ISSN 0968-4328. doi: 10.1016/j.micron.2012.03.020.
- [10] P. Blaha, K. Schwarz, G. Madsen, D. Kvasnicka, and J. Luitz. Wien2k, an augmented plane wave + local orbitals program for calculating crystal properties, 2001. URL <http://www.wien2k.at>. (Karlheinz Schwarz, Techn. Universität Wien, Austria).
- [11] Earl J. Kirkland. *Advanced computing in electron microscopy*. Plenum Press, 1998. ISBN 0-306-45936-1.
- [12] P. Schattschneider, M. Stger-Pollach, S. Löffler, A. Steiger-Thirsfeld, J. Hell, and J. Verbeeck. Sub-nanometer free electrons with topological charge. *Ultramicroscopy*, 115(0):21 – 25, 2012. ISSN 0304-3991. doi: 10.1016/j.ultramic.2012.01.010.
- [13] Ján Rusz, Olle Eriksson, Pavel Novák, and Peter M. Oppeneer. Sum rules for electron energy loss near edge spectra. *Phys. Rev. B*, 76(6):060408, 2007. doi: 10.1103/PhysRevB.76.060408.
- [14] Kevin Jorissen. *The ab initio calculation of relativistic electron energy loss spectra*. PhD thesis, Universiteit Antwerpen, 2007.
- [15] P. Hansmann, M. W. Haverkort, A. Toschi, G. Sangiovanni, F. Rodolakis, J. P. Rueff, M. Marsi, and K. Held. Atomic and itinerant effects at the transition-metal x-ray absorption  $k$  pre-edge exemplified in the case of  $\text{V}_2\text{O}_3$ . *Phys. Rev. B*, 85:115136, Mar 2012. doi: 10.1103/PhysRevB.85.115136.